PAPER • **OPEN ACCESS**

Quantum study of halogen substituted anti-b18h22 borane clusters for optoelectronics

To cite this article: Mahmoud Deeb *et al* 2025 *Phys. Scr.* **100** 055403

Physica Scripta

PAPER

Quantum study of halogen substituted anti-b18h22 borane clusters for optoelectronics

Mahmoud Deeb[1,5], **Nabil Joudieh**[1,2,5], **Nidal Chamoun**[3,4,5,*] and **Habib Abboud**[2,5]

[1] Department of Physics, University of Damascus, Damascus, Syria
[2] Faculty of Pharmacy, IUST, Daraa Highway, Ghabagheb, Damascus, Syria
[3] Arabic Language Academy of Damascus, P.O. Box 327, Bld 6, AbdulMunim Riadh St., Malki Damascus, Syria
[4] CASP, Antioch Syrian University, Maaret Saidnaya, Damascus, Syria
[5] These authors contributed equally to this work.
[*] Author to whom any correspondence should be addressed.

E-mail: mahmoud.deeb311@hotmail.com, njoudieh@yahoo.fr, chamoun@uni-bonn.de and Habib-abboud@iust.edu.sy

Keywords: DFT, TD-DFT, UV–vis, IR, Raman, anti-$B_{18}H_{22}$, Laser Borane

OPEN ACCESS

RECEIVED
2 December 2024

REVISED
9 March 2025

ACCEPTED FOR PUBLICATION
17 March 2025

PUBLISHED
11 April 2025

Abstract

We offer a quantum chemical analysis of mono-halogenated borane molecules using DFT and TD-DFT theories, applying the PBE0/def2-SVPD and B3LYP/6-311+G(d) methods as implemented in ORCA, and explore how solvent effects influence electronic transition properties. The comparable benchmarks are the archetype anti-$B_{18}H_{22}$ denoted as (1) against hypothetical halogenated derivatives: 7-F-anti-$B_{18}H_{21}$ (2), 4-F-anti-$B_{18}H_{21}$ (3), and the recently synthesized 4-Br-anti-$B_{18}H_{21}$ (4). The analysis includes an optimization of the ground and first singlet excited states, vibrational frequency analysis, and a comprehensive spectroscopic profile covering IR, Raman, UV-Vis absorption, and emission spectra. The IR spectra of the fluorinated compounds feature a characteristic B-F stretching peak, while the Raman spectra closely resemble the parent molecule. UV-Vis spectral analysis shows a redshift and oscillator strength enhancement for F at position B7, indicating altered electronic properties due to substitution with lighter halogen. Furthermore, solvent effects enhance the probability of electronic transitions. Halogene presence led to a decrease of the energy gap EG(LUMO-HOMO) due to the stabilization of LUMO, which implied a redshift in the emission/absorption wavelength spectra, with the largest EG change at around 14% occurring for the (4)*th* benchmark compound.. Notably, all compounds emit light within the visible spectrum, underscoring their potential for optoelectronic applications.

1. Introduction

Boron compounds have recently attracted considerable attention due to their wide-ranging applications in various fields. Among the binary boranes, which consist primarily of boron and hydrogen, the anti-$B_{18}H_{22}$ isomer is particularly notable for its unique fluorescence properties and a quantum yield nearing unity. The photophysical characteristics of this isomer were first uncovered by Londesborough and his team in an experimental study that was supported by theoretical computational analysis of its excited states [1].

The first derivative of this isomer, anti-$B_{18}H_{20}(HS)_2$, was synthesized through chemical substitution. This modification significantly enhanced singlet oxygen production, increasing the quantum yield from 0.0008 in the original compound to 0.59 in the substituted version [2].

Additionally, the first inorganic laser based on the anti-$B_{18}H_{22}$ molecule was developed, with its solutions displaying pulsed laser emission in the blue spectral range and achieving an efficiency of 9.5 % [3]. This breakthrough has paved the way for further research into anti-$B_{18}H_{22}$ derivatives aimed at enhancing their photophysical properties.

Researchers have since synthesized and characterized a new di-substituted derivative, anti-$B_{18}H_{20}(NC_5H_5)_2$. In solution, this derivative exhibited fluorescence emission in the range of 650-690 nm, though with a low

quantum yield of 0.003. However, in the solid state, the fluorescence wavelength experienced a blueshift to 585 nm, and the quantum yield of fluorescence significantly increased to 0.15 [4, 5].

The borane compound was treated with iodine, resulting in the formation of mono- and di-halogenated derivatives: 7-I-anti-$B_{18}H_{21}$ and 4,4'-I_2-anti-$B_{18}H_{20}$. The mono-iodinated derivative exhibited green phosphorescence at 525 nm with a quantum yield of 0.41. In contrast, the di-iodinated derivative showed a wavelength shift to 545 nm and a higher quantum yield of 0.71. The experimental absorption spectra of both iodinated compounds were similar to that of anti-$B_{18}H_{22}$, with a redshift of approximately 30 nm due to iodine's influence. Theoretical analysis using the CASPT2 method aligned well with experimental values for vertical absorption and emission energies [6]. The optical stability of the compound 4,4′-I_2-anti-$B_{18}H_{20}$ is better than that of 7-I-anti-$B_{18}H_{21}$, whereas the radiative lifetime τ_0 of the latter (27 μs) largely exceeds the former's (2.4 μs) due to the di-halogenated derivative containing two iodine atoms enhancing the spin–orbit coupling, and thus more probable intersystem crossing processes, and hence decreasing the excited state lifetime. The quantum yield of singlet oxygen photosensitiazation is higher in the mono(0.52)- than the di(0.36)-iodinated derivative, whereas both compounds are highly luminescent, exhibiting effective green phosphorescence, where emissions could be quenched via dioxygen with high quantum yield. These good efficiencies in the photophysical processes make these two compounds promising photosensitizers of dioxygen.

Bromination of anti-$B_{18}H_{22}$ produced the mono-halogenated derivative 4-Br-anti-$B_{18}H_{21}Br$, which exhibited dual emission: fluorescence at 410 nm and phosphorescence at 503 nm. Computational analysis, utilizing the hybrid functional PBE0 and the DZP basis set with relativistic effects, showed good agreement between theoretical calculations and experimental data for both absorption and emission spectra [7]. The substituted compound absorbs light at 343 nm with a molar absorptivity less than that of the original one by around 72%. The dual emission emerges from a delicate balance between populating the two levels T_1 and S_1, which is provided for by the substituting Br. Quenching the phosphorescence signal is achieved by raising the Oxygen content in the cyclohexane solution, whereas the fluorescence signal is not affected by Oxygen, which allows for the possibility of using this derivative as a ratiometric oxygen probe.

Recently, alkylated borane derivatives were synthesized, demonstrating high stability, solubility, and unique fluorescence properties. These compounds emit blue light in the range of 423–427 nm with a quantum yield of 0.71 to 1. Their UV absorption, spanning 283–357 nm, closely mirrors that of the parent compound (anti-$B_{18}H_{22}$), with a redshift of around 10 nm. Theoretical analysis using the CASPT2 method was performed to explore the photophysical properties of the anti-$B_{18}H_{18}(CH_3)_4$ and anti-$B_{18}H_{18}(C_2H_5)_4$ compounds. The calculated results showed a strong correlation with the experimental values for vertical absorption and emission energies [8].

Upon methylation of anti-$B_{18}H_{22}$, an increase in the polyhedral volume was observed, leading to the formation of anti-$B_{18}H_8C_{l2}(CH_3)_{12}$. This substitution enhanced the absorption and solubility properties of the fluorescent molecule. Compared to anti-$B_{18}H_{22}$, there is a redshift of approximately 30 nm in the absorption bands and 20 nm in the emission bands, indicating significant changes in the molecule's photophysical properties [9].

The size swelling of the substituted Boran substructure is caused by the electronic density decrease in the cluster due to the electron withdrawing effect by the more electronegative Carbon atoms. Absorption coefficient increases by around 20% compared to that of the original compound, whereas the fluorescence quantum yield lags behind, at 76%, but still too high compared to other familiar standards in the field.

The compound anti-$B_{18}H_{20}(NC_9H_7)_2$, formed by the addition of isoquinoline to anti-$B_{18}H_{22}$, exhibited notable aggregation-induced emission in tetrahydrofuran/water. It absorbs light between 370–500 nm and shows a red-shifted absorption peak compared to its precursor. Its fluorescence spectrum across various solvents shows a single peak within 616–680 nm, with the solvent having minimal effect on the absorption and emission peaks [10].

In a recent study, a halogenation reaction of the borane compound produced mono-halogenated derivatives, specifically 4-I-anti-$B_{18}H_{21}$ and 7-Cl-anti-$B_{18}H_{21}$. Spectroscopic analysis revealed that the iodinated derivative displayed phosphorescence at a wavelength of 514 nm with a quantum yield of 0.16. In contrast, the chlorinated derivative exhibited fluorescence emission at a shorter wavelength of 418 nm, achieving a quantum yield of 0.80, the highest recorded among all halogenated borane derivatives reported to date [11].

The compound 4-I-anti-$B_{18}H_{21}$ shows an absorption similar to that of the original compound, but with a molar absoptivity less by 35%, similar to the case of 7-I-anti-$B_{18}H_{21}$. It emits a green phosphorescence at 514 nm with a quantum yield (0.16), less than its 7-I-anti-$B_{18}H_{21}$ counterpart (0.41). As to the compound 7-Cl-anti-$B_{18}H_{21}$, it emits light at 344 nm with a molar absorptivity larger by 20% than that of the original one, whereas its fluorescence occurs at 418 nm with quantum yield (0.80). These data show that the absorption coefficient, the emission wavelength and the nature of luminescence (phosphorescence vs fluorescence) depend on the substituting atom identity, whereas the quantum yield depends more on the substitution position.

By treating the original compound by $AlCl_3$ in Tetrachloromethane solutions, one gets various Chlorine substituted derivatives [12]. The compound 3-Cl-anti-$B_{18}H_{21}$ (3,3'-Cl_2-anti-$B_{18}H_{20}$, 4,4'-Cl_2-anti-$B_{18}H_{20}$) absorbs light at 327 (324, 344) nm, with fluorescence at 407 (410, 435) nm, with quantum yield of 0.52 (0.07, 0.17) and fluorescence lifetime of 6.1 (1.2, 1.5) ns. The study showed that the increase of the number of chlorine atoms implies a decrease in the fluorescence quantum yield as well as in its lifetime. Substitution at the B3, B3' positions reduces the fluorescence efficiency more than the case of B4, B4'. Moreover, substitution at B4 leads to a larger (smaller) redshift (fluorescence quenching) than that corresponding to B3 substitution. Also, substitution at B7 is more stable compared to those of B3 or B4, but it provides a better quantum yield, since the Chlorine atom leads to reducing the excited states lifetime, whence the probability of their absorption of the pumpingstimulated emission energies decreases, a factor which plays a major role in worsening the performance of Boran laser [13].

Since the light halogen Cl showed the highest quantum yield among all halogenated boranes up to date , and led to molar absorptivity which exceeds the parent compound's one, it is logical and important to explore the effects of the lightest halogen F on the photophysical properties of laser borane. Furthermore, we aim to complete analysing the halogens substitutions, in that the Br, I and Cl have been studied recently, with no mention of F and At, so it was natural to study these two elements, which was not done previously. While the calculations of the latter (At) are underway, the analysis of F substitutions forms an integral part of this work. Past studies did not discuss, neither the IR and Raman spectra, nor the thermodynamical properties of Borane. Thus, our results can be helpful in designing a Borane-derivative apt for future optoelectronics applications requiring certain wavelengths and refined thermodynamical conditions.

Building on existing research, we have conducted a theoretical investigation using computational chemistry to explore the properties that arise when a hydrogen atom in anti-$B_{18}H_{22}$ is replaced by a halogen atom. The goal of this study is to uncover the structural and photophysical changes that such substitutions can trigger in borane compounds. We examined the hypothetical fluorinated molecules 7-F-anti-$B_{18}H_{21}$ and 4-F-anti-$B_{18}H_{21}$, alongside the parent molecule anti-$B_{18}H_{22}$ and the recently synthesized brominated derivative 4-Br-anti-$B_{18}H_{21}$. For this work, we have used hyprid functionals which can afford a good result in balance offering a compromise between the accuracy and the computational costs.

Previous studies have shown that sites B4 and B7 are the most favored sites for halogen substitution. According to reference [7], the borane heads B4 and B4' are the most electron-rich and therefore the most likely to undergo electrophilic substitution. Moreover, the similarities in reaction conditions for producing iodine- and chlorine-substituted compounds at site B7, such as the absence of a catalyst, suggest that the preference for substitution site can be determined by the intermediate reactive species arising from halogen conditions [11]. Most previous studies were limited to halogenations at sites 4 and 7, and we stick in this work to this choice.

The plan of the paper is as follows. In section 2, we present the computational methods that we used. The results are presented in section 3, including the optimised ground state geometry in section 3.1, and the HOMO and LUMO orbitals in section 3.2, followed by a study of the vibrational modes of IR and Raman spectroscopies in section 3.3, while presenting the TD-DFT calculation in section 3.4 covering the vertical emission and absorption energies as well as the adiabatic and 0-0 ones. We end up by concluding remarks in section 4. An appendix states all the vertical absorption wavelengths and corresponding oscillation strengths using various methods.

2. Computational methods

In this study, quantum chemical calculations were carried out using the ORCA software package (version 5.0.2) [14]. The PBE0 hybrid functional and the def2-SVP basis set were utilized for optimizing molecular geometries and analyzing IR and Raman spectra [15, 16]. Optimization of the first excited singlet state (S_1) was performed with the def2-SVPD basis set. To calculate the vertical transition energies for the first ten excited singlet states, TD-DFT calculations were conducted using two methods: PBE0/def2-SVPD [17] and B3LYP/6-311+G(d) [18, 19] in both gas phase and solvent phase (Hexane) with the CPCM model [20]. Molecular structures were visualized, and atom numbering was adjusted using Chemcraft software to ensure consistency with previous studies [21]. Moreover, the spectroscopic analysis were processed using Python.

PBE0 method is built on theoretical parameters, which makes it more universal in computation. Furthermore, it proved effective in the past Bromine-substituted compound study [7]. On the other hand, B3LYP is built on experimental parameters, and is widely used in quantum computations, and also proved to be successful when applied to calculate the equilibrium geometry of the original compound [1]. The basis def2-SVP was sufficient to compute the equilibrium geometries of the ground state, and it was successful in obtaining valid structures. From the other side, the two bases def2-SVPD and 6-311+G(d) provided, both, similar accuracies in calculation, as they both use diffuse functions, which provides for a more precise description of the excited

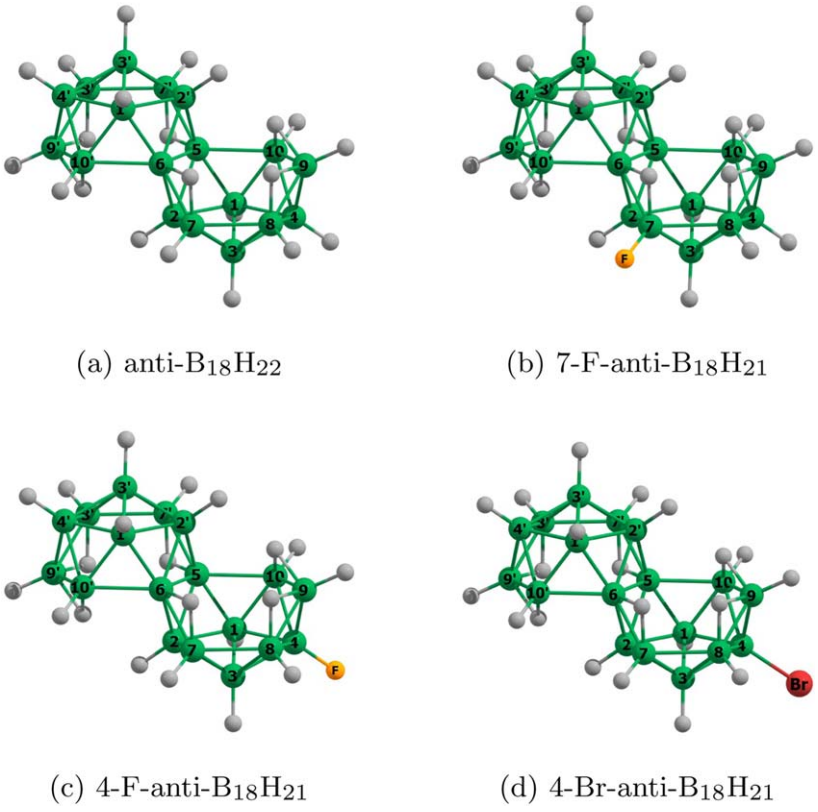

Figure 1. Optimized S_0 geometry with atoms numbering.

states. Finally, we chose the CPCM model, amidst the ORCA available models including the sophisticated SMD and the obsolete COSMO, as it is a compromise between good accuracy and heavy computational cost. We adopted the Hexane solvent since it was used in the previous study of the original compound, which would make the comparison easier.

3. Results and discussion

3.1. Optimized ground state geometry

The ground-state geometric configuration for each molecule (figure 1) was precisely optimized using the PBE0 hybrid functional combined with the def2-SVP basis set, as implemented in the ORCA computational chemistry software. Generally, the molecular geometry remains mostly unchanged upon substitution, with only slight expansions and contractions observed in the boron-boron bond lengths near the substitution sites. In the compounds 7-F-anti-$B_{18}H_{21}$ (1), 4-F-anti-$B_{18}H_{21}$ (2), and 4-Br-anti-$B_{18}H_{21}$ (3), the most significant bond elongations were found in the B8-B7, B4-B9, and B4-B1 bonds, respectively, with deviations from the anti-$B_{18}H_{22}$ (1) reference molecule being 0.027, 0.013, and 0.006 Å, respectively. Conversely, the most contracted bonds for (2), (3), and (4) were B4-B8, B8-B7, and B8-B7, respectively. These bonds showed changes in bond length compared to the parent compound of −0.010, −0.006, and −0.005 Å, respectively, highlighting the significant impact of the substitutions at these specific molecular positions. Table 1 presents the bond lengths for the studied molecules at their optimized ground-state geometries, whereas figure 2 shows the maximal deviations δ in B-B bonds between the halogenated derivatives and the parent compound, at their S_0 geometries.

Looking at figure 2, we see that the shapes, for the ground state, of the bond length changes are somehow similar for the substituted compounds at 4-F and 4-Br. However the latter bonds are mostly shorter than the former, which suggests that the substitution by Br leads to a more stable structure. As to the 7-F-substitution compound, it has the longest elongation, compared to the parent compound, exceeding 0.025 A^o.

3.2. *HOMO* and *LUMO* orbitals

The Highest Occupied Molecular Orbital (HOMO) and the Lowest Unoccupied Molecular Orbital (LUMO) play a crucial role in determining a molecule's photophysical properties, stability, and electronic characteristics.

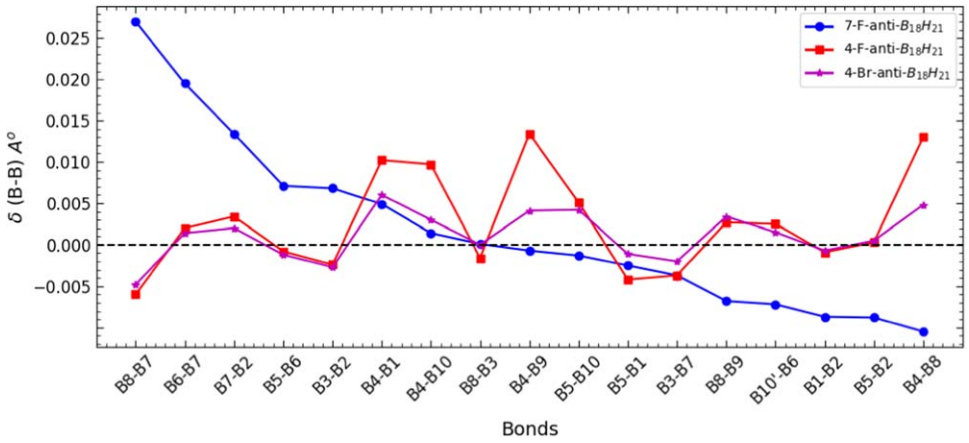

Figure 2. Maximal differences δ in B-B bonds between halogenated derivatives and parent compund, at their S_0 geometries.

Table 1. Bonds lengths for all derivatives compared to parent molecule.

Bonds	anti-$B_{18}H_{22}$	7-F-anti-$B_{18}H_{21}$		4-F-anti-$B_{18}H_{21}$		4-Br-anti-$B_{18}H_{21}$	
	d(B-B) (A^o)	d(B-B) (A^o)	$\delta(A^o)$	d(B-B) (A^o)	$\delta(A^o)$	d(B-B) (A^o)	$\delta(A^o)$
B8-B7	1.9522	1.9792	0.0270	1.9462	−0.0060	1.9474	−0.0048
B6-B7	1.8145	1.8340	0.0195	1.8165	0.0020	1.8159	0.0014
B7-B2	1.7873	1.8007	0.0134	1.7907	0.0034	1.7893	0.0020
B5-B6	1.8028	1.8099	0.0071	1.8020	−0.0008	1.8016	−0.0012
B3-B2	1.7589	1.7657	0.0068	1.7565	−0.0024	1.7562	−0.0027
B4-B9	1.7231	1.7224	−0.0007	1.7365	0.0134	1.7272	0.0041
B4-B8	1.8016	1.7911	−0.0105	1.8146	0.0130	1.8064	0.0048
B4-B1	1.7919	1.7968	0.0049	1.8021	0.0102	1.7979	0.0060
B4-B10	1.7805	1.7819	0.0014	1.7902	0.0097	1.7835	0.0030
B4-B3	1.7781	1.7796	0.0015	1.7848	0.0067	1.7815	0.0034
B5-B10	1.9598	1.9585	−0.0013	1.9649	0.0051	1.9640	0.0042
B5-B2	1.8023	1.7935	−0.0088	1.8026	0.0003	1.8028	0.0005
B1-B2	1.7822	1.7735	−0.0087	1.7813	−0.0009	1.7815	−0.0007
B10′-B6	1.9604	1.9532	−0.0072	1.9629	0.0025	1.9619	0.0015
B8-B9	1.7936	1.7868	−0.0068	1.7963	0.0027	1.7970	0.0034
B5-B1	1.7573	1.7548	−0.0025	1.7531	−0.0042	1.7562	−0.0011
B3-B7	1.7569	1.7532	−0.0037	1.7532	−0.0037	1.7549	−0.0020
B8-B3	1.7503	1.7504	0.0001	1.7487	−0.0016	1.7503	0.0000
B4-(F/Br)	—	—	—	1.3613	—	1.9557	—
B7-F	—	1.346020	—	—	—	—	—

The energy gap (EG) between the HOMO and LUMO, commonly referred to as the band gap, is a key parameter that significantly affects the absorption and emission spectra, and is defined as: ($EG = E_{LUMO} - E_{HOMO}$).

The brominated molecule (4) exhibits the smallest energy gap, while the parent molecule (1) has the largest. For example, the fluorinated molecule at position B7 (2) shows an energy gap difference of approximately 0.03 eV compared to the fluorinated molecule at position B4. In contrast, the brominated molecule (4) has an energy gap that differs by about 0.42 eV from that of molecule (3). This suggests that the type of substituted atom has a significant effect on the energy gap, whereas the position of the substituted atom has a more subtle impact on *EG*. These results highlight the critical role that both the type and position of substituted atoms play in determining molecular energy gaps. The energy gap (EG) values for the molecules studied are detailed in table 2, providing valuable insights into the electronic properties of these compounds.

3.3. Vibrational modes: IR and raman spectrum

In order to determine the normal modes of vibration, one needs to compute the spectral eigenvalues of the free energy Hessian, which give the vibration frequencies. Minima correspond to all these frequencies being positive, whereas any negative value would correspond either to a maximum or a saddle point. In our case, we found all the vibrational frequencies are positive, whence energy stability is guaranteed.

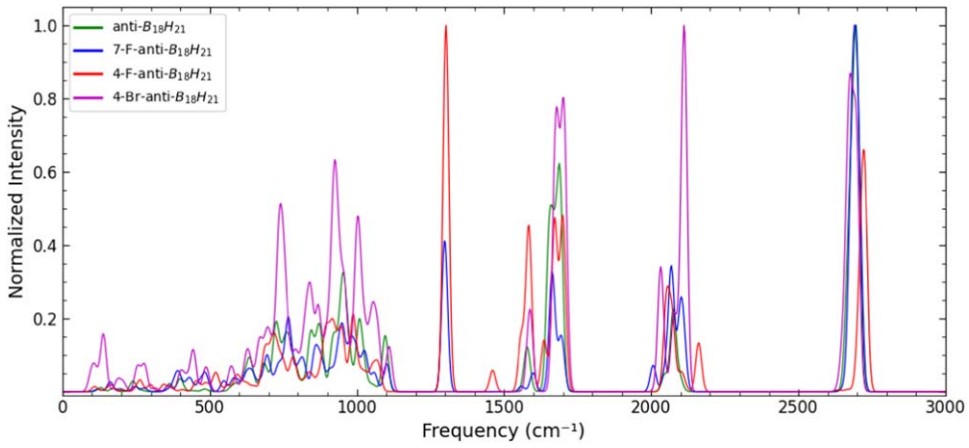

Figure 3. Calculated IR spectrum for all molecules.

Table 2. HOMO, LUMO, and Energy Gap (*EG*) at S_0 geometry, with PBE0/def2-SVPD level of theory.

Compound	*HOMO* (*ev*)	*LUMO* (*ev*)	*EG* (*ev*)
anti-$B_{18}H_{22}$	−7.963 [−7.874]	−3.203 [−3.104]	4.760 [4.769]
7-F-anti-$B_{18}H_{21}$	−7.933 [−7.837]	−3.249 [−3.142]	4.684 [4.696]
4-F-anti-$B_{18}H_{21}$	−7.983 [−7.882]	−3.327 [−3.208]	4.656 [4.675]
4-Br-anti-$B_{18}H_{21}$	−7.650 [−7.671]	−3.407 [−3.282]	4.243 [4.389]

The values in brackets were calculated with CPCM(Hexane) model.

Table 3. Spectral regions of vibration modes and corresponding molecular motions.

Frequency Range (cm^{-1})	Type of motion
2500–3000	B-H Bonds Stretching
2000–2500	B-H Bonds Stretching in B-H-B Bridge
1500–2000	B-H Bonds Bending in B-H-B Bridge
< 1500	Complex Motions and Fingerprint Region

Frequency calculations were performed at the same theoretical level as that used for optimization. Each molecule exhibits 114 vibrational modes within the far and mid-infrared spectrum. These vibrational modes have been systematically categorized into four distinct spectral regions, each corresponding to specific molecular motions. The spectral range of 2500–3000 cm^{-1} is associated with B-H bond stretching, while the B-H bond stretching within the B-H-B bridge is most prominent in the 2000–2500 cm^{-1} region. Additionally, B-H bond bending within the B-H-B bridge is evident in the 1500–2000 cm^{-1} interval. The region below 1500 cm^{-1} encompasses more complex molecular motions and is recognized as the fingerprint region of the spectrum. Table 3 outlines the four spectral regions and the corresponding types of molecular motions.

The infrared (IR) spectrum of the halogenated molecules showed minimal deviations from that of the parent compound (1). This comes from the fact that the derivatives have the same general form of the configurations of laser borane anti-$B_{18}H_{22}$, with the exception of an additional strong peak observed exclusively in the fluorinated derivatives (2) and (3). This peak is attributed to the stretching of the B-F bond. In contrast, the brominated derivative did not exhibit this peak. Comparative spectral analysis revealed that the IR spectrum of compound (4) is characterized by a more pronounced peak below 1500 cm^{-1}, a feature linked to B-Br bond stretching vibrations in this region, in addition to a stronger peak around 2200 cm^{-1}, due to B-H stretching in B-H-B bridges near the Br atom.

Figure 3 presents the IR spectra of all three derivatives alongside that of compound (1), providing a visual comparison that highlights both the similarities and differences in the spectra. The substitution of atoms within the molecule invariably affects the IR spectrum, as vibrational frequencies are sensitive to changes in atomic

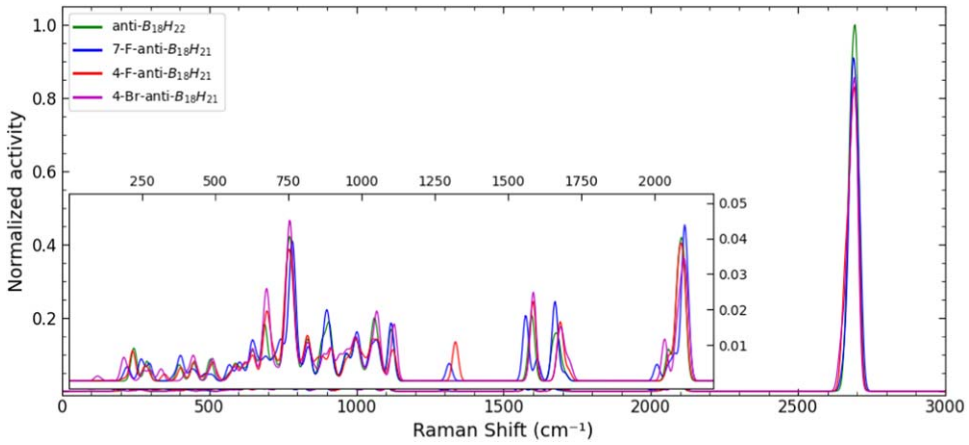

Figure 4. Calculated Raman activity spectrum for all four molecules.

Table 4. Active vibrational modes in IR spectra.

Mode	anti-$B_{18}H_{22}$		7-F-anti-$B_{18}H_{21}$		4-F-anti-$B_{18}H_{21}$		4-Br-anti-$B_{18}H_{21}$	
	Freq (cm^{-1})	Int (km/mol)	Freq (cm^{-1})	Int (km/mol)	Freq (cm^{-1})	Int (km/mol)	Freq (cm^{-1})	Int (km/mol)
66	932.48	10.55	929.57	12.26	925.11	28.56	923.96	110.67
92	1575.25	24.26	1298.5	305.49	1319.79	319.99	1110.64	13.39
94	1653.6	144.87	1598.94	37.78	1585.87	47.17	1589.65	45.65
95	1670.53	113.92	1658.71	20.53	1673.97	144.28	1673.61	137.36
96	1689.17	165.41	1664.12	222.24	1679.75	44.74	1684.9	88.09
97	1693.1	42.46	1690.33	58.66	1698.08	148.39	1703.79	188.02
98	2045.41	15.94	1698.38	62.15	1706.76	150.49	1714.71	1.66
100	2074.89	79.98	2046.78	37.77	2053.28	75.59	2035.36	29.6
101	2078.68	0.24	2068.52	249.14	2073.83	62.14	2075.93	48.06
104	2660.43	11.79	2110.38	88.27	2104.39	42.61	2112.13	253.82
116	2694.28	42.07	2695.76	251.49	2689.84	45.88	2691.25	25.26
119	2702.98	100.37	2710.57	169.12	2702.35	34.74	2699.53	68.59

mass and bond strength. Consequently, changes in the type or position of substituted atoms can lead to significant shifts in these frequencies, thereby influencing the IR spectrum. As one can notice from figure 3, compound (2) showed its strongest peak around 2700 cm^{-1}, which is assigned to B-H stretching, while compound (3) has the strongest peak around 1200 cm^{-1}, which is attributed to B-F elongation. This variation between position B7 for (2) and position B4 for (3) can be assigned to the higher electronegativity of B4, which leads to extra change in polarity, thus to a stronger peak in IR spectrum. We also show in table (4) the active vibrational IR modes for the four compounds, stating their frequencies and intensities confirming numerically what is noted qualitatively in figure 3.

Numerical frequency calculations were performed, leading to the determination of Raman activities. Raman activity is the difference in intensity between stoke's (Photon loss energy) and anti-stoke's (Photon gain energy) scattering. All molecules exhibited a prominent peak within the 2600–2700 cm^{-1} spectral range, corresponding to various symmetrical stretching of the B-H bonds, However, all other modes were not active in Raman spectra, a fact which arises because most of these modes are bending or asymmetrical stretching, leading thus to an insufficient change in molecule polarizability. Actually, in the infrared spectrum, a distinct peak was observed for fluorinated molecules, attributed to B-F stretching vibrations, though it displayed minimal Raman activity. Notably, this peak is absent in both the parent molecule (1) and the brominated molecule (4). Figure 4 presents the complete Raman Activity spectrum in comparison with molecule (1).

The Raman intensity data were calculated using Chemcraft software, with laser radiation at 18797 cm^{-1}, which is the optimal frequency for investigating inorganic molecules, at a temperature of 298.15 K. Upon comparing the Raman activity spectrum, reliant on the Raman scattering intensity difference between left- and right-circularly polarized light due to molecular chirality, several peaks exhibited enhanced intensity in the Raman intensity spectrum, particularly in the region below 1200 cm^{-1}. These changes indicate increased

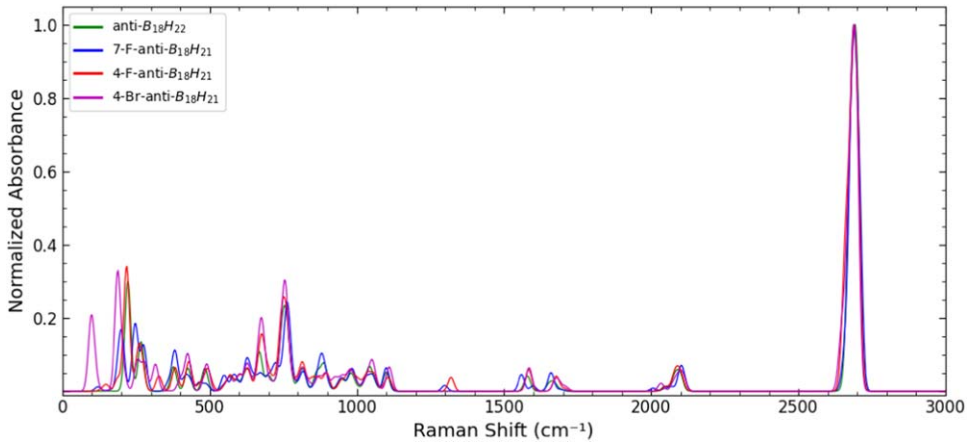

Figure 5. Calculated raman intensity spectrum for all molecules, laser radiation = 18797 cm^{-1} at 298.15 K.

Table 5. Thermodynamics properties at $T = 298.15$ K and $P = 1$ *atm*.

Molecule	Electronic E_{el} (*Eh*)	Entropy(*Eh*)	Enthalpy (*Eh*)	Gibbs G (*Eh*)	$G - E_{el}$ (*Eh*)	$C_{V,vib}$ (J/K.mole)
anti-$B_{18}H_{22}$	−459.78178	0.05091	−459.469371	−459.52028	0.26150	280.24
7-F-anti-$B_{18}H_{21}$	−558.90979	0.05306	−558.60264	−558.65571	0.25408	291.55
4-F-anti-$B_{18}H_{21}$	−558.90578	0.05295	−558.59895	−558.65190	0.25387	292.52
4-Br-anti-$B_{18}H_{21}$	−3032.76923	0.05526	−3032.46356	−3032.51883	0.25039	296.96

favourability of the corresponding vibrational modes at the selected laser wavelength. Moreover, looking at the relation between activity S_i and intensity R_i in Raman spectra (equation (1), where ν_i is the frequency of the i_{th} mode, ν_0 is the laser frequency, and K, T, c, h are Boltzman's constant, temperature, speed of light and Planck's constant, respectively)

$$R_i = \frac{(2\pi)^2}{45}(\nu_0 - \nu_i)^4 \times \frac{h}{8\pi^2 c\nu_i(1 - e^{-\frac{h\nu_i c}{KT}})} \times S_i \quad (1)$$

justifies the existence of intense peaks below 1500 cm^{-1}, despite their weak activity, since ν being in the denominator leads to large Raman intensity at smaller frequencies regardless of the activity. Furthermore, compound (4) showed a unique peak around 100 cm^{-1}, which can be attributed to the movement of the heavy bromine atom. Figure 5 displays the Raman intensity spectrum for the studied molecules.

Finally, the frequency calculations provided thermodynamic properties (covering the electronic energy, entropy, enthalpy, Gibbs, and vibrational heat capacity), which are summarized in table 5.

Thermodynamic properties play an important role in determining the thermal stability of compounds, where those of negative enthalpy tend to be more stable, which would make them useful in optoelectronic devices working at high temperatures. Table 5 shows a clear increase in Enthalpy and in Gibbs free energy in halogenated compounds, in particular those corresponding to Bromine substitution, predicting thus a better thermal stability.

The slight differences in entropy values are due to the original Borane structure being kept by the substituted compounds, which lead to similar vibrational entropies. The largest vibrational entropy leads to coupling between the electronic and vibrational levels, which enhances the non-radiative relaxation processes competing with the radiative ones. As to the large differences in Enthalpy and Gibbs free energy, they are caused by the large discrepancies in the compounds electronic energies, which result from the increasing interaction of electrons with nuclei and other electrons in the presence of halogens, the most pronounced of which corresponds to Bromine substitution. The higher electronic energy in the bromine-substituted compound is due to its heavy bromine atom, including a larger number of electrons leading, thus, to more interactions amidst electrons and nuclei. A larger absolute value of electronic energy means a more challenging task of breaking up the compound, thus a better stability, although other factors, such as bond lengths and formation energy, play also a role.

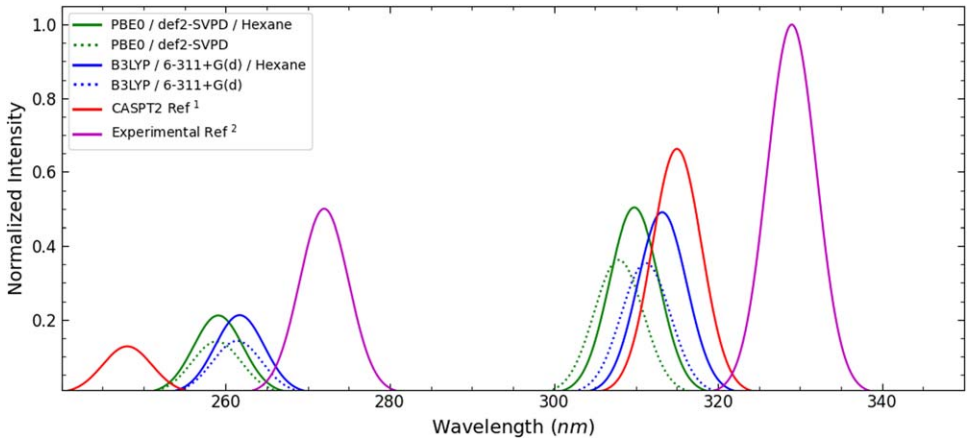

Figure 6. Calculated UV–vis spectra for anti-$B_{18}H_{22}$ in comparison with previous work. [1]Calculated at CASPT2 level of theory on MOLCAS software [1]. [2]Measure in hexane [1].

The vibrational heat capacity was computed using the following statistical formula:

$$C_{V,vib} = R\sum_{i=1}^{\alpha}\left[\left(\frac{h\nu_i}{K_B T}\right)^2 \frac{e^{-\frac{h\nu_i}{K_B T}}}{(1 - e^{-\frac{h\nu_i}{K_B T}})^2}\right] \quad (2)$$

where, α is the number of vibrational modes, ν_i is the frequency of the *ith* mode, T is the temperature and R, K_B, and h are ideal gas, Boltzman, and Planck constants, respectively. Heat capacities play an essential role in optoelectronic devices, where materials with higher values can manage thermal changes better, maintaining stable performance under varying operating conditions.

3.4. TD-DFT calculation

In computational chemistry, exploring excited states is crucial for understanding the photophysical properties of compounds. Time-dependent density functional theory (TDDFT) is an essential tool for simulating electronic transitions. In this study, we employed TDDFT to evaluate the optimized geometry of the first singlet excited state (S_1) and to calculate the vertical absorption and emission energies, offering theoretical insights that correspond well with experimental findings. We utilized two methods, PBE0/def2-SVPD and B3LYP/6-311+G (d), in both the gas phase and solvent phase using Hexane with the CPCM model.

3.4.1. Vertical absorption energies

In our research, we conducted TD-DFT calculations to validate the vertical absorption energies of excited states. The results for the parent compound (1) closely matched experimental data on absorption wavelengths, although a discrepancy was observed in the oscillator strength compared to previous calculations. The oscillator strength for the transition to the second excited state (S_2) was minimal. However, the oscillator strength for the initial absorption aligned well with values calculated using the more accurate CASPT2 method. Incorporating solvent effects with the CPCM (Hexane) model increased the probability of the transition, though the transition to S_2 remained negligible. Table 6 presents the first three transitions, comparing them to results from previous research [1].

Also, we show in figure 6 the calculated UV–vis spectra for the anti-$B_{18}H_{22}$ compound compared to previous work [1] quoting both calculations done with CASPT2 in MOLCAS software and measurements in hexane.

As to the fluorinated molecules, their transition energies showed minimal deviation from those of compound (1), with a slight redshift of approximately 8 nm. The oscillator strength values for compound (2) were similar to those of compound (1). In contrast, compound (3) exhibited a significantly increased oscillator strength for the transition to the S_2 state, which was negligible in both compounds (1) and (2), while compound (2) (Flourinated at B7) showed the highest *f* value among all studied molecules. This indicates an enhancement in molar absorptivity, which is compatible with the highest absorbency when substituted with Cl at position B7 in a previous study [11]. Theoretically, it is worth mentioning that the larger the oscillator strength *f* for specific transition between two states is, the more similar the corresponding wave functions are.

On the other hand, using CPCM (Hexane) model enhanced the transition probabilities, as reflected in the oscillator strength values shown in table 7, which compares the first three vertical absorption wavelengths for the fluorinated molecules (2) and (3) with those of the parent molecule (1).

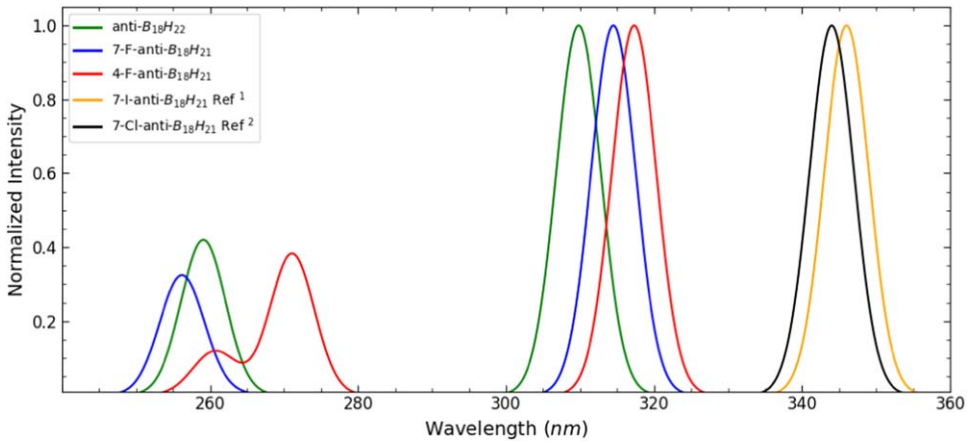

Figure 7. Calculated UV–vis spectra for flourinated derivatives in comparison with the previous halgenated at position B7. **Notes:** Calculations carried out at PBE0/def2-SVPD/Hexane level of theory, and normalized for the highest oscillator strength for each spectra, separately: [1]Previous halogenated 7-I-anti-$B_{18}H_{21}$ [6]. [2]Previous halogenated 7-Cl-anti-$B_{18}H_{21}$ [11].

Table 6. Vertical absorption energy for anti-$B_{18}H_{22}$ in comparison with previous work [1].

State	PBE0 def2-SVPD[a]		B3LYP 6-311+G(d)[a]		CASPT2 [1][b]		Exp [1]
	$\lambda_{VA}(nm)$	f	$\lambda_{VA}(nm)$	f	$\lambda_{VA}(nm)$	f	$\lambda_{abs}(nm)$
S_1	308 [310]	0.143 [0.201]	311 [313]	0.141 [0.196]	315	0.265	329
S_2	263 [262]	0.000 [0.000]	264 [263]	0.000 [0.000]	248	0.051	272
S_3	259 [259]	0.055 [0.084]	261 [261]	0.056 [0.084]	212	0.884	215

λ_{VA} is the calculated vertical absorption wavelength at S_0 geometry, f is the oscillator strength. λ_{abs} is the experimental absorption wavelength observed in hexane solution. The values in brackets were calculated with CPCM model in Hexane.

[a] As obtained in ORCA 5.0 (this work).

[b] As obtained in MOLCAS 7.0 (previous work [1]).

Actually, the transition probability of the main absorption peak, corresponding to vertical transition from S0 to S1, increased in Hexane of about 40% for compounds (1), (2), and (3), whereas significant enhancement occured for the compound (4) reaching about 90% due to more polarity caused by bromine atom. This suggests a solvent-cluster interaction of the Van der Waals-type, since the solvent is non-polar.

Likewise, we show in figure 7 our calculated UV–vis spectra for the fluorinated derivatives compared to halogenated compounds at B7 position previously quoted ([6] for I and [11] for Cl).

The brominated molecule exhibited a redshift in its absorption wavelength of approximately 47 nm, accompanied by a lower oscillator strength compared to the parent compound (1). The bromine-substituted compound exhibits a greater redshift than the fluorine-substituted ones, which signifies a reduction in the energy required to excite the former molecule. The calculated vertical absorption energies closely matched the experimental data [7]. Using the PBE0/def2-SVPD method, the first transition to S_1 at 354 nm corresponds well with the experimental peak observed at 341 nm, while the transition to S_2 at 295 nm aligns with the peak around 300 nm. When using the B3LYP/6-311+G(d) method, the transitions were redshifted but still in good agreement with experimental observations. The best agreement was achieved by using the CPCM (Hexane) model with the PBE0/def2-SVPD method. Table 8 presents the vertical absorption wavelengths, comparing them with previous experimental and calculated data. As illustrated in figure 8, our calculated values align more closely with the experimental data, even though we did not include relativistic effects, which were considered in previous studies [7].

In tables (6–8), we limited, for presentation purposes, the results to the first three states. However the full results for all the states appear in appendix. Tables A1(A2) shows the results using PBE0 in gas (solvent) phase, whereas table A3 corresponds to using B3LYP in both phases.

3.4.2. Vertical emission energies

We optimized the geometry of the first singlet excited state (S_1) for each molecule. For compounds (1) and (2), the most significant elongation was observed in the B9-B10 and B9′-B10′ bonds, with a change of approximately

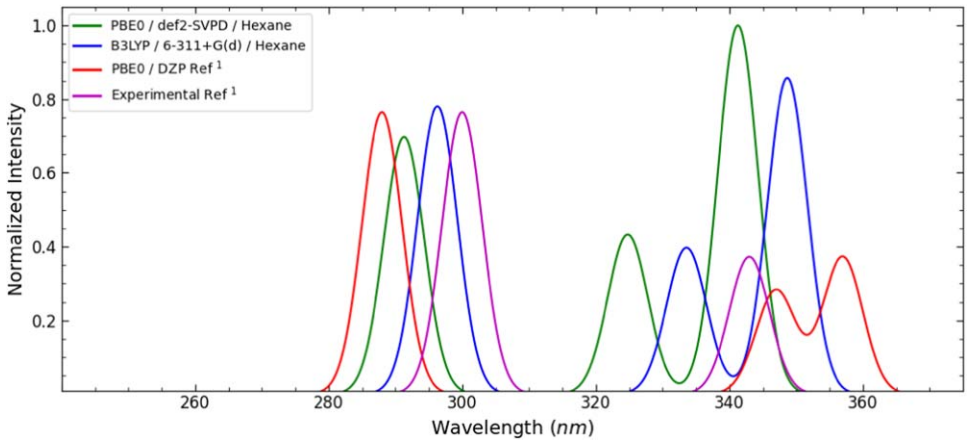

Figure 8. Calculated UV–vis for brominated derivative in comparison with previous work [7]. Note: [1]Calculated with scalar relativistic effects in ADF software. Measured in cyclohexane [7].

Table 7. Vertical absorption energy for flourinated molecules compared to parent compound.

State	anti-$B_{18}H_{22}$		7-F-anti-$B_{18}H_{21}$		4-F-anti-$B_{18}H_{21}$	
	$\lambda_{VA}(nm)$	f	$\lambda_{VA}(nm)$	f	$\lambda_{VA}(nm)$	f
			PBE0 def2-SVPD			
S_1	308 [310]	0.1448 [0.2014]	312 [315]	0.1637 [0.2229]	316 [317]	0.1457 [0.2022]
S_2	263 [262]	0.0000 [0.0000]	262 [262]	0.0009 [0.0014]	272 [271]	0.0533 [0.0774]
S_3	259 [259]	0.0564 [0.0846]	256 [256]	0.0470 [0.0720]	261 [261]	0.0176 [0.0240]
			B3LYP 6-311+G(d)			
S_1	311 [313]	0.1415 [0.1962]	316 [318]	0.1637 [0.2157]	320 [321]	0.1407 [0.1951]
S_2	264 [263]	0.0000 [0.0000]	264 [263]	0.0006 [0.0011]	275 [274]	0.0539 [0.0778]
S_3	261 [261]	0.0569 [0.0849]	259 [259]	0.0468 [0.0715]	264 [264]	0.0138 [0.0189]

$\lambda_{V\,A}$ is the calculated vertical absorption wavelength at S_0 geometry, f is the oscillator strength. No previous experimental nor theoretical data available for those two new derivatives. Again, the values in brackets were calculated with CPCM model in Hexane solvent.

Table 8. Vertical absorption energies for 4-Br-anti-$B_{18}H_{21}$.

State	PBE0 def2-SVPD[a]		B3LYP 6-311+G(d)[a]		PBE0 DZP [7][b]		Exp [7]
	$\lambda_{VA}(nm)$	f	$\lambda_{VA}(nm)$	f	$\lambda_{VA}(nm)$	f	$\lambda_{abs}(nm)$
S_1	354 [341]	0.0627 [0.1189]	363 [349]	0.0527 [0.1019]	357	0.0443	343
S_2	341 [325]	0.0367 [0.0514]	351 [334]	0.0341 [0.0472]	347	0.0336	343
S_3	295 [291]	0.0809 [0.0829]	299 [296]	0.0861 [0.0928]	288	0.0909	300

λ_{VA} is the calculated vertical absorption wavelength at S_0 geometry, f is the oscillator strength. λ_{abs} is the experimental absorption wavelength observed in hexane solution. The values in brackets were calculated with CPCM model in Hexane.

[a] As obtained in ORCA software without Relativistic effects (this work).

[b] As obtained in ADF with Relativistic effects (previous worke [7]).

0.05 Å. The most substantial contraction occurred in the B6-B10′ bond, with a difference of around 0.1 Å. In compounds (3) and (4), the B9-B10 bond exhibited the maximum elongation, with a change of approximately 0.09 Å. Compound (3) also showed maximum contraction in the B6-B10′ bond with a difference of about 0.1 Å. For compound (4), the B5-B10 and B7-B8 bonds experienced the most significant contractions, with changes of approximately 0.12 Å. Table 9 provides a detailed comparison of the top three changes in B-B bond lengths between the optimized geometries of S_1 and S_0.

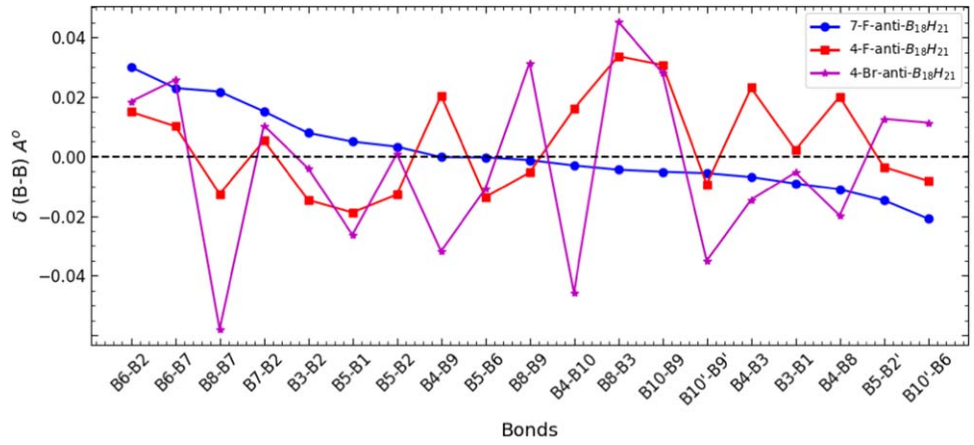

Figure 9. Maximal differences δ in B-B bonds between halogenated derivatives and parent compound, at their S_1 geometries.

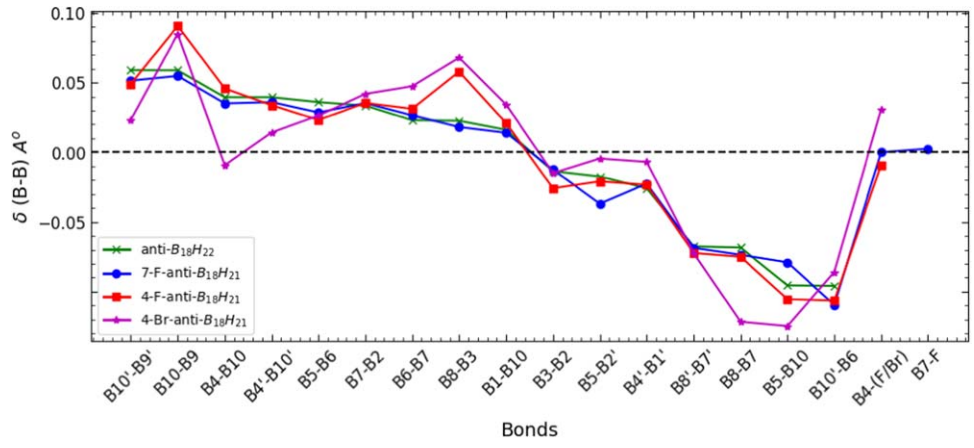

Figure 10. Maximal differences δ in B-B bonds between S_1 and S_0 geometries for each molecule under this study.

Table 9. Differences, δ in B-B bonds length between S_1 and S_0 geometries.

Bond	anti-$B_{18}H_{22}$ $\delta(s_1 - s_0)$ A^o	7-Fanti-$B_{18}H_{21}$ $\delta(s_1 - s_0)$ A^o	4-F-anti-$B_{18}H_{21}$ $\delta(s_1 - s_0)$ A^o	4-Br-anti-$B_{18}H_{21}$ $\delta(s_1 - s_0)$ A^o
B5-B10	−0.0955	−0.079	−0.1054	−0.1247
B7-B8	−0.0684	−0.0736	−0.075	−0.1216
B6-B10′	−0.0958	−0.1095	−0.1065	−0.0859
B4-B10	0.0395	0.0351	0.0458	−0.0093
B4′-B10′	0.0395	0.036	0.0338	0.0142
B9′-B10′	0.0589	0.0514	0.049	0.0233
B7-B6	0.023	0.0265	0.0312	0.0474
B3-B8	0.0226	0.0181	0.0579	0.0679
B9-B10	0.0588	0.0548	0.0907	0.085
B7-F	—	0.0026	—	—
B4-F	—	—	−0.0091	—
B4-Br	—	—	—	0.0308

In figure 9, we show the maximal deviations in B-B bonds between halogenated derivatives and the parent compound. Likewise, figure 10 shows these deviations between the S_1 and S_0 geometries for each studied molecule.

Additionally, the energies of the HOMO and LUMO orbitals changed at the S_1 optimized geometry, resulting in a general decrease in the energy gap (EG). Compounds (1) and (3) exhibited an EG difference of approximately −0.8 eV, while compounds (3) and (4) showed a change in EG values of approximately −0.9 eV.

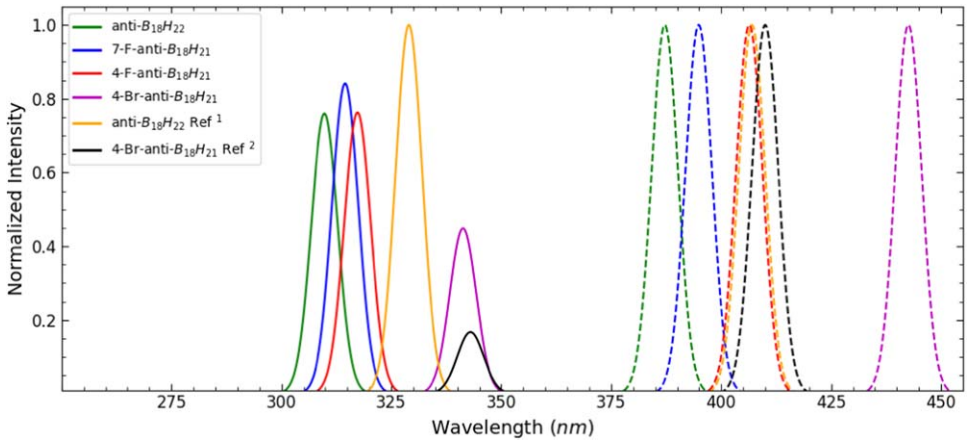

Figure 11. Absorption and Emission spectra calculated at PBE0/def2-SVPD/Hexane level of theory, in comparison with previous data. Notes: Absorption denoted as solid line, emission as dashed line, and previous work in orange, and black for compound (1), and (4), respectively. Absorption intensities were normalized for the max oscillator strength of compound (1) in the previous work [1], whereas emission intensities were normalized separately. [1]In hexane [1]. [2]In cyclohexane [7].

Table 10. HOMO, LUMO and EG energy gap at S_1 geometry, with PBE0/def2-SVPD level of theory.

Compound	*HOMO* (*ev*)	*LUMO* (*ev*)	*EG* (*ev*)
anti-$B_{18}H_{22}$	−7.674 [−7.585]	−3.760 [−3.661]	3.914 [3.925]
7-F-anti-$B_{18}H_{21}$	−7.645 [−7.550]	−3.815 [−3.707]	3.830 [3.843]
4-F-anti-$B_{18}H_{21}$	−7.657 [−7.562]	−3.914 [−3.795]	3.743 [3.767]
4-Br-anti-$B_{18}H_{21}$	−7.460 [−7.520]	−4.097 [−3.969]	3.363 [3.551]

The values in brackets were calculated with CPCM(Hexane) model.

These changes contribute to a redshift in emission energy, as evidenced by the vertical emission energy calculations. The EG values for all studied molecules at their S_0 and S_1 geometries are presented in table 10.

Energy gaps play an important role in determining the compounds optical physical properties, and one can consider them as first approximations of excitation energies. The smaller the energy gap is, the larger the redshift in absorption wavelength becomes, a fact which would contribute to diminishing the energy required to excite the compounds.

Based on the optimized S_1 geometry, we conducted time-dependent density functional theory (TD-DFT) calculations to determine the vertical emission energies. Figure 11 displays the normalized absorption and emission spectra for all molecules calculated at PBE0/def2-SVPD/Hexane level of theory, in comparison with previous data ([1] for hexane solvent and [7] for cyclohexane).

Our analysis revealed that all compounds emitted light within the visible spectrum. Notably, the fluorinated derivatives (2) and (3) exhibited slight redshifts, while the brominated derivative (4) demonstrated a significant redshift of approximately 100 nm compared to compound (1).

Compound (1) has a vertical emission wavelength (λ_{VE}) of 383 nm, showing a redshift of 75 nm from the vertical absorption wavelength (λ_{VA}). This result aligns well with the observed peak around 407 nm and the calculated peak of 426 nm at the CASPT2 level of theory [1]. Furthermore, the fluorinated molecules (2) and (3) displayed vertical emissions at 390 nm and 404 nm, respectively, with redshifts of 78 nm and 87 nm. The brominated molecule exhibited the highest vertical emission wavelength at 473 nm, although this value deviates significantly from both experimental and calculated data.

We hypothesize that this discrepancy may result from the exclusion of relativistic effects associated with the heavy bromine atom. Including a solvent model (CPCM in Hexane) improved the agreement with previous experimental and theoretical values, especially for the brominated derivative (4). For radiative lifetime, calculated using the Strickler-Berg equation [22], the values were in good agreement for compound (1) with the experimental data, but an overestimation was observed for the brominated compound (4). However, closer values were obtained by incorporating the CPCM (Hexane) model, as shown in table 11, which details the vertical emission energies and the excited state's lifetime. It is worth mentioning that compound (1), which has laser emission, is not the one with the highest τ values. This comes since longer radiative lifetimes might lead to other processes occurring, which can negatively affect the efficiency of the laser.

Table 11. Vertical emission wavelength and radiative lifetime.

Compound	$\lambda_{VA}\,(nm)$	$\lambda_{VE}\,(nm)$	$\tau\,(ns)$	$\lambda_{abs}\,(nm)$	$\lambda_{F}\,(nm)$	$\tau_{F}\,(ns)$
	PBE0 def2-SVPD				Exp	
anti-$B_{18}H_{22}$	308 [310]	383 [387]	13.7 [10.5]	329[a]	407[a]	11.2[a]
7-F-anti-$B_{18}H_{21}$	312 [315]	390 [394]	13.4 [10.4]	—	—	—
4-F-anti-$B_{18}H_{21}$	316 [317]	404 [406]	14.8 [11.3]	—	—	—
4-Br-anti-$B_{18}H_{21}$	354 [341]	473 [442]	78.5 [34.4]	341[b]	410[b]	10.6[b]
	B3LYP 6-311+G(d)				Theo	
anti-$B_{18}H_{22}$	311 [313]	386 [390]	13.91 [10.7]	315[a]	426[a]	5.6[a]
7-F-anti-$B_{18}H_{21}$	316 [318]	394 [399]	13.75 [10.7]	—	—	—
4-F-anti-$B_{18}H_{21}$	320 [321]	408 [410]	15.38 [11.7]	—	—	—
4-Br-anti-$B_{18}H_{21}$	363 [349]	490 [457]	101.9 [44.1]	357[b]	374[b]	—

λ_{VA} vertical absorption wavelength, λ_{VE} vertical emission wavelength, τ radiative lifetime in nanosecond. λ_{abs} absorption wavelength, λ_{F} flourescence wavelngth and τ_{F} flourescence lifetime. Exp experimental and Theo theoretical previous values. The values in bracket were calculated with CPCM(Hexane) model.

[a] Experimental values measured in hexane, and calculated at CASPT2 level of theory [1].

[b] Measured in cyclohexane, and calculated at PBE0/DZP with scalar relativistic effect [7].

Table 12. Adiabatic and origin band energies.

Compund	PBE0/def2-SVPD		B3LYP/6-311+G(d)	
	$\lambda_{adia}\,(nm)$	$\lambda_{0-0}\,(nm)$	$\lambda_{adia}\,(nm)$	$\lambda_{0-0}\,(nm)$
anti-$B_{18}H_{22}$	340 [344]	351 [355]	347 [350]	358 [362]
7-F-anti-$B_{18}H_{21}$	346 [350]	357 [362]	353 [357]	365 [370]
4-F-anti-$B_{18}H_{21}$	353 [356]	365 [369]	359 [362]	373 [375]
4-Br-anti-$B_{18}H_{21}$	405 [383]	419 [396]	422 [398]	438 [412]

λ_{adia} adiabatic wavelength, λ_{0-0} origin band wavelength. The values in bracket were calculated with CPCM(Hexane) model.

The overestimation of the excited state lifetime using the 'Strickler-Berg' formula:

$$\tau = \frac{1}{2.142005 E_{\mathrm{VE}}^{3}\,\mathrm{TDM}^{2}} \tag{3}$$

is due to two factors. First, the transition dipole moment TDM, related to oscillator strength, is of small value in Bromine substituted compound, which, due to its existence in the denominator, was argued to give overestimating values [22]. Second, the vertical emission energy E_{VE} enters the formula raised to the cubic power making it of paramount effect. The fact that the estimation was done for emission wavelength at 442 nm, whereas the experimental one is at 410 nm, leads to reducing E_{VE} and overestimating the lifetime. Moreover, neglecting relativistic effects led to an additional underestimation (overestimation) of $E_{\mathrm{VE}}\,(\tau)$.

3.4.3. Adiabatic and 0-0 energies

Table 12 shows the adiabatic energies λ_{adia} and origin band energies λ_{0-0}. Adiabatic energy is the difference between S_0 and S_1 energies at their respective geometries, while origin band energy is the energy difference between the lowest vibrational energy state in S_0 and that for S_1, which can be calculated by adding the difference in zero-point vibration energy between S_0 and S_1, to the adiabatic energy [23]. The origin band energy calculated in this study is in good agreement with the experimental value 364 nm and better than the theoretical value calculated at CASPT2 level of theory 341 nm [1].

4. Conclusion

In summary, our work delves into the quantum chemical analysis of mono-halogenated borane molecules utilizing DFT and TD-DFT methods. We compare the archetypal anti-$B_{18}H_{22}$ with hypothetical halogenated derivatives: 7-F-anti-$B_{18}H_{21}$, 4-F-anti-$B_{18}H_{21}$, and the recently synthesized 4-Br-anti-$B_{18}H_{21}$. Our

comprehensive study includes optimizations of ground state and first singlet excited state geometries, vibrational frequency analysis, and detailed spectroscopic characterization. The fluorinated compounds display distinct features in the IR spectra, while the brominated compound exhibits a unique peak in the Raman spectra. UV-Vis analysis highlights changes in electronic properties due to halogenation, and all studied compounds emit visible light, indicating their potential for optoelectronic applications. Ultimately, using ORCA software with the PBE0/def2-SVPD and B3LYP/6-311+G(d) methods, alongside the CPCM model, achieves accuracy comparable to the more computationally demanding CASPT2 method. This convergence significantly streamlines the theoretical investigation, particularly for the brominated derivative.

One can substitute other halogens in the used two positions, in order to study the effects of the substituting atom identity and the substitution site on the spectral properties of Borane Laser.

All studied compounds were found to emit visible light, suggesting their potential for optoelectronic applications. Actually, one can signal two impacts of shifts in absorption peaks, the first on wavelength range which may widen under halogenation, which is crucial for applications like solar cells with broader absorption spectrums improving efficiency, whereas the second relates to changes in the absorption intensity, shown by the damping coefficient, with higher intensity meaning better light-harvesting capabilities, essential for light-emitting devices. As to the shift in emission peaks, it allows for color tuning which is important for display technologies and lighting applications. The best halogenated compound is revealed to be the compound (2) with F-substituted at site 7, because it has the highest absorptivity, in a similar way to the Cl-substituted compound studied previously and which showed a better quantum yield when compared to other halogenated compounds.

Supplementary information

Acknowledgments

N. C. acknowledges support from the CAS PIFI fellowship and from the Humboldt Foundation.

Data availability statement

All data that support the findings of this study are included within the article (and any supplementary files).

Appendix. Vertical absorption wavelengths and corresponding oscillator strength

Table A1. Vertical absorption wavelengths and corresponding oscillator strength *f*. Using PBE0 / def2-SVPD.

br State	anti-$B_{18}H_{22}$		7-F-anti-$B_{18}H_{21}$		4-F-anti-$B_{18}H_{21}$		4-Br-anti-$B_{18}H_{21}$	
	λ_{VA}	f	λ_{VA}	f	λ_{VA}	f	λ_{VA}	f
S_1	307.9	0.1448	312.3	0.1637	316.1	0.1458	354	0.0627
S_2	263.3	0.0000	262	0.0009	272.3	0.0533	341.1	0.0368
S_3	258.9	0.0564	256.1	0.0471	261.2	0.0176	294.5	0.0809
S_4	248.2	0.0000	248.3	0.0027	246.8	0.0119	257.6	0.024
S_5	240.7	0.0275	240.8	0.0144	243.1	0.0017	251.4	0.0065
S_6	232.9	0.0000	234.9	0.0006	235.7	0.0166	247.7	0.0024
S_7	230.4	0.0164	230.3	0.0296	233.2	0.0012	243.8	0.0046
S_8	229.2	0.0000	229	0.0088	229.9	0.0215	236.5	0.0377
S_9	226.6	0.0346	223.4	0.0039	228.3	0.0061	234.6	0.0071
S_{10}	224.8	0.0000	221.4	0.0002	225.8	0.0041	231.9	0.0033
T_1	376.9	forbidden	384.9	forbidden	387.1	forbidden	403.3	forbidden
T_2	288.3	forbidden	290.2	forbidden	304.9	forbidden	359.6	forbidden
T_3	286.7	forbidden	284	forbidden	291.7	forbidden	327.9	forbidden
T_4	267	forbidden	264.5	forbidden	262.3	forbidden	277.7	forbidden
T_5	256.2	forbidden	254.8	forbidden	255.9	forbidden	271.5	forbidden
T_6	248.8	forbidden	251.2	forbidden	251.6	forbidden	264.1	forbidden
T_7	243.1	forbidden	245.3	forbidden	249.5	forbidden	256.1	forbidden
T_8	240.2	forbidden	237.7	forbidden	240.3	forbidden	251.7	forbidden
T_9	237.5	forbidden	232	forbidden	237.3	forbidden	241.5	forbidden
T_{10}	232	forbidden	231.8	forbidden	234.7	forbidden	240.4	forbidden

$\lambda_{V\,A}$ vertical absorption wavelength, *f* oscillator strength.

Table A2. Vertical absorption wavelengths and corresponding oscillator strength *f*. Using PBE0 / def2-SVPD / Hexane.

State	anti-$B_{18}H_{22}$		7-F-anti-$B_{18}H_{21}$		4-F-anti-$B_{18}H_{21}$		4-Br-anti-$B_{18}H_{21}$	
	λ_{VA}	f	λ_{VA}	f	λ_{VA}	f	λ_{VA}	f
S_1	309.8	0.2014	314.5	0.2229	317.3	0.2022	341.3	0.1189
S_2	262.3	0.0000	261.5	0.0015	271.1	0.0774	324.8	0.0515
S_3	259.1	0.0846	256.2	0.0721	260.7	0.024	291.3	0.0829
S_4	247.8	0.0000	247.1	0.0032	246	0.0176	256.9	0.037
S_5	240.2	0.0453	240.1	0.0247	242.1	0.0034	249.9	0.0056
S_6	232.1	0.0000	234.3	0.0009	234.9	0.0289	246.8	0.0073
S_7	229.5	0.0304	230.3	0.0489	232.6	0.0039	239.5	0.0059
S_8	229	0.0000	228.1	0.0068	229.6	0.0317	235.6	0.0498
S_9	226.5	0.0409	223	0.0052	227.6	0.0048	231.2	0.0021
S_{10}	224.3	0.0000	220.9	0.0001	225.2	0.0052	228.6	0.0092
T_1	375.9	forbidden	383.6	forbidden	385.3	forbidden	395.1	forbidden
T_2	287.8	forbidden	289.5	forbidden	302.7	forbidden	343.1	forbidden
T_3	286	forbidden	283.7	forbidden	290.6	forbidden	318.2	forbidden
T_4	265.4	forbidden	262.7	forbidden	261	forbidden	275.4	forbidden
T_5	255.7	forbidden	254.1	forbidden	255	forbidden	268.6	forbidden
T_6	248.4	forbidden	250.8	forbidden	251.1	forbidden	262.9	forbidden
T_7	242.3	forbidden	244.7	forbidden	248.4	forbidden	253.9	forbidden
T_8	239.2	forbidden	236.4	forbidden	239.4	forbidden	249.9	forbidden
T_9	236.3	forbidden	231.5	forbidden	236.2	forbidden	240.3	forbidden
T_{10}	231.3	forbidden	231.4	forbidden	233.7	forbidden	237.5	forbidden

$\lambda_{V\,A}$ vertical absorption wavelength, *f* oscillator strength.

Table A3. Vertical absorption wavelengths and corresponding oscillator strength *f*. Using B3LYP / 6-311+G(d).

State	anti-$B_{18}H_{22}$		7-F-anti-$B_{18}H_{21}$		4-F-anti-$B_{18}H_{21}$		4-Br-anti-$B_{18}H_{21}$	
	λ_{VA}	f	λ_{VA}	f	λ_{VA}	f	λ_{VA}	f
S_1	311.2 [313.2]	0.1415 [0.1962]	316 [318.2]	0.1587 [0.2157]	319.7 [320.9]	0.1407 [0.1951]	362.6 [348.7]	0.0527 [0.1020]
S_2	264 [263.2]	0.0000 [0.0000]	263.9 [263.4]	0.0007 [0.0011]	275.2 [273.9]	0.0540 [0.0778]	350.5 [333.6]	0.0341 [0.0472]
S_3	261.4 [261.7]	0.0569 [0.0849]	258.9 [259.1]	0.0469 [0.0715]	264.1 [263.5]	0.0138 [0.0190]	298.8 [296.3]	0.0861 [0.0928]
S_4	249 [248.4]	0.0000 [0.0000]	249.4 [248.1]	0.0020 [0.0023]	247.2 [246.3]	0.0098 [0.0138]	259.8 [259.1]	0.0255 [0.0396]
S_5	241.1 [240.4]	0.0173 [0.0285]	241.1 [240.3]	0.0079 [0.0138]	243.7 [242.6]	0.0006 [0.0010]	253.3 [251.4]	0.0057 [0.0072]
S_6	234.5 [234.1]	0.0000 [0.0000]	239.3 [238.7]	0.0001 [0.0002]	237.9 [237.3]	0.0020 [0.0029]	250.9 [248.1]	0.0025 [0.0032]
S_7	231.1 [230.4]	0.0000 [0.000]	230.7 [230.8]	0.0266 [0.0409]	235.4 [234.5]	0.0130 [0.0258]	247.4 [244.6]	0.0031 [0.0045]
S_8	230.5 [229.7]	0.0154 [0.0305]	228.9 [227.9]	0.0022 [0.0028]	230.1 [229.8]	0.0170 [0.0236]	241.8 [236.6]	0.0227 [0.0371]
S_9	226.9 [226.6]	0.0241 [0.0271]	224.2 [223.9]	0.0027 [0.0039]	229.8 [229.1]	0.0007 [0.0002]	237.2 [233.4]	0.0092 [0.0156]
S_{10}	225.9 [225.4]	0.0000 [0.0000]	221.3 [220.9]	0.0002 [0.0003]	226.6 [226]	0.0053 [0.0069]	231.8 [231.1]	0.0014 [0.0071]
T_1	376.6 [375.8]	- [-]	384.9 [383.7]	- [-]	386.9 [385.1]	- [-]	405.8 [396.8]	- [-]
T_2	288 [287.5]	- [-]	290.5 [289.8]	- [-]	304.6 [302.4]	- [-]	366.4 [349]	- [-]
T_3	286.2 [285.6]	- [-]	284 [283.7]	- [-]	292.1 [290.9]	- [-]	332.6 [323]	- [-]
T_4	265.3 [263.7]	- [-]	263.1 [261.3]	- [-]	260.9 [259.5]	- [-]	278.7 [276.8]	- [-]
T_5	253.9 [253.3]	- [-]	253.8 [253.1]	- [-]	255.6 [254.7]	- [-]	272.9 [270.1]	- [-]
T_6	249.6 [249.3]	- [-]	252.2 [251.5]	- [-]	251.6 [250.6]	- [-]	262.3 [261]	- [-]
T_7	242.2 [241.5]	- [-]	244.6 [244]	- [-]	248.3 [247.6]	- [-]	259.5 [255.8]	- [-]
T_8	238.1 [237.2]	- [-]	236 [234.9]	- [-]	239.8 [238.9]	- [-]	250.6 [249.5]	- [-]
T_9	236 [234.8]	- [-]	234.7 [234.3]	- [-]	237.5 [236.6]	- [-]	246.5 [240.1]	- [-]
T_{10}	233.1 [232.4]	- [-]	232.7 [232.3]	- [-]	235 [234]	- [-]	242.4 [238.4]	- [-]

λ_{VA} vertical absorption wavelength, *f* oscillator strength. The values in brackets were calculated with CPCM model in Hexane solvent.

ORCID iDs

Mahmoud Deeb https://orcid.org/0009-0006-7086-2302
Nidal Chamoun https://orcid.org/0000-0002-6140-643X

References

[1] Londesborough M G, Hnyk D, Bould J, Serrano-Andres L, Sauri V, Oliva J M, Kubat P, Polivka T and Lang K 2012 Distinct photophysics of the isomers of B18H22 explained *Inorg. Chem.* **51** 1471–9
[2] Saurì V, Oliva J M, Hnyk D, Bould J, Braborec J, Merchan M, Kubat P, Cisarova I, Lang K and Londesborough M G 2013 Tuning the photophysical properties of anti-B18H22: Efficient intersystem crossing between excited singlet and triplet states in new 4,4′-(hs)2-anti-B18H20 *Inorg. Chem.* **52** 92669274
[3] Cerdán L, Braborec J, Garcia-Moreno I, Costela A and Londesborough M G 2015 A borane laser *Nat. Commun.* **6** 5958
[4] Londesborough M G *et al* 2017 Thermochromic fluorescence from b18h20 (nc5h5) 2: an inorganic-organic composite luminescent compound with an unusual molecular geometry *Adv. Opt. Mater.* **5** 1600694
[5] Londesborough M G, Dolanský J, Jelìnek T, Kennedy J D, Cìsařová I, Kennedy R D, Roca-Sanjuán D, Francés-Monerris A, Lang K and Clegg W 2018 Substitution of the laser borane anti-b 18 h 22 with pyridine: a structural and photophysical study of some unusually structured macropolyhedral boron hydrides *Dalton Trans.* **47** 1709–25
[6] Londesborough M G *et al* 2019 Effect of iodination on the photophysics of the laser borane anti-b18h22: generation of efficient photosensitizers of oxygen *Inorg. Chem.* **58** 10248–59
[7] Anderson K P, Waddington M A, Balaich G J, Stauber J M, Bernier N A, Caram J R, Djurovich P I and Spokoyny A M 2020 A molecular boron cluster-based chromophore with dual emission *Dalton Trans.* **49** 16245–51
[8] Bould J *et al* 2020 A series of ultra-efficient blue borane fluorophores *Inorg. Chem.* **59** 17058–70
[9] Londesborough M G, Lang K, Clegg W, Waddell P G and Bould J 2020 Swollen polyhedral volume of the anti-b18h22 cluster via extensive methylation: Anti-b18h8cl2me12 *Inorg. Chem.* **59** 2651–4
[10] Chen J, Xiong L, Zhang L, Huang X, Meng H and Tan C 2020 Synthesis, aggregation-induced emission of a new anti-b18h22-isoquinoline hybrid *Chem. Phys. Lett.* **747** 137328
[11] Anderson K P, Rheingold A L, Djurovich P I, Soman O and Spokoyny A M 2022 Synthesis and luminescence of monohalogenated b18h22 clusters *Polyhedron* **227** 116099
[12] Ehn M, Bavol D, Bould J, Strnad V, Litecká M, Lang K, Kirakci K, Clegg W, Waddell P G and Londesborough M G 2023 A window into the workings of anti-b18h22 luminescence—blue-fluorescent isomeric pair 3, 3′-cl2-b18h20 and 3, 4′-cl2-b18h20 (and others) *Molecules* **28** 4505
[13] Cerdan L, Francés-Monerris A, Roca-Sanjuán D, Bould J, Dolanský J, Fuciman M and Londesborough M G 2020 Unveiling the role of upper excited electronic states in the photochemistry and laser performance of anti-b 18 h 22 *Journal of Materials Chemistry* C **8** 12806–18
[14] Neese F 2012 The orca program system *Wiley Interdisciplinary Reviews: Computational Molecular Science* **2** 73–8
[15] Campo J M, Gázquez J L, Trickey S and Vela A 2012 Non-empirical improvement of pbe and its hybrid pbe0 for general description of molecular properties *J. Chem. Phys.* **136** 104108
[16] Weigend F and Ahlrichs R 2005 Balanced basis sets of split valence, triple zeta valence and quadruple zeta valence quality for h to rn: design and assessment of accuracy *Phys. Chem. Chem. Phys.* **7** 3297–305
[17] Rappoport D and Furche F 2010 Property-optimized gaussian basis sets for molecular response calculations *J. Chem. Phys.* **133**
[18] Becke A D 1993 Density functional thermochemistry. iii. the role of exact exchange *J. Chem. Phys.* **98** 5648–52
[19] Curtiss L A, McGrath M P, Blaudeau J-P, Davis N E, Binning R C and Radom L 1995 Extension of gaussian-2 theory to molecules containing third-row atoms ga-kr *J. Chem. Phys.* **103** 6104–13
[20] Barone V and Cossi M 1998 Quantum calculation of molecular energies and energy gradients in solution by a conductor solvent model *The Journal of Physical Chemistry* A **102** 1995–2001
[21] Zhurko G and Zhurko D 2025 http://chemcraftprog.comChemcraft
[22] Strickler S and Berg R A 1962 Relationship between absorption intensity and fluorescence lifetime of molecules *J. Chem. Phys.* **37** 814–22
[23] Katan C, Savel P, Wong B M, Roisnel T, Dorcet V, Fillaut J-L and Jacquemin D 2014 Absorption and fluorescence signatures of 1, 2, 3-triazole based regioisomers: challenging compounds for td-dft *Phys. Chem. Chem. Phys.* **16** 9064–73